

Supporting Information

Ideal Strength and Deformation Mechanism in Inorganic Halide Double Perovskite $\text{Cs}_2\text{AgBiBr}_6$

Xiaohan Liu^{1,2}, Yabin Ren⁴, Shihao Wang^{1,2}, Yingzhuo Lun³, Bo Yang^{4*}, Bonan Zhu³,
Jiawang Hong^{3*}, Gang Tang^{1,2*}

¹Beijing Institute of Technology, Zhuhai Beijing Institute of Technology (BIT)

Zhuhai 519088, P.R.China

²School of Interdisciplinary science, Beijing Institute of Technology, Beijing 100081,

China

³School of Aerospace Engineering, Beijing Institute of Technology, Beijing, 100081,

China

⁴School of Mechanical Engineering, State Key Laboratory of Reliability and

Intelligence Electrical Equipment National Engineering, Hebei University of

Technology, Tianjin 300401, China

*E-mails:

Bo Yang: boyang@hebut.edu.cn;

Jiawang Hong: hongjw@bit.edu.cn;

Gang Tang: gtang@bit.edu.cn.

S1 Computational Methods

Our Density Functional Theory (DFT) calculations were performed using the *Vienna Ab initio Simulation Package* (VASP) and the Projector-Augmented Wave (PAW) method¹⁻³, with the following pseudopotentials: PAW_PBE Cs_sv 08Apr2002, PAW_PBE Ag 02Apr2005, PAW_PBE Bi 08Apr2002, and PAW_PBE Br 06Sep2000. Total energy calculations and geometry optimization were conducted using the Perdew-Burke-Ernzerhof (PBE) exchange-correlation functional⁴. We employed both the Generalized Gradient Approximation (GGA) and the hybrid Heyd-Scuseria-Ernzerhof (HSE06)^{5,6} combining with SOC function methods to investigate the impact of strain on the electronic band structure, including variations in the band gap, while simultaneously studying the optical properties of the structure.

To study the structural response to strain, we first unload the applied shear strain, that is, release the applied strain until the stress drops to zero, and then fully optimize the structure using VASP. During the optimization process, we do not impose any symmetry constraints (i.e., ISYM = 0 in the VASP setting), allowing the system to spontaneously break the symmetry based on the interaction between atoms and the principle of energy minimization. Phenomena such as octahedral rotation or phase transition may naturally occur. If the optimized structure cannot restore to the initial structural symmetry, we consider a phase transition has occurred. During this process, the symmetry of the structure is determined by the FINDSYM software⁷.

Structural optimization was carried out with a $4 \times 4 \times 4$ k -point grid in \mathbf{k} -space integration, using a plane-wave basis set with a kinetic energy cutoff of 600 eV. All atomic positions were relaxed until all remaining force components were below 0.005 eV/Å. We calculate the dielectric constants ϵ_∞ and ϵ_0 using density functional perturbation theory (DFPT)⁸, as well as the effective phonon frequency ω and carrier effective mass m^* as implemented in the AMSET package⁹. The crystal orbital Hamilton population (COHP) and crystal orbital bond index (COBI) analyses are conducted using the LOBSTER package^{10,11}. The force constant calculations were performed using the PHONOPY software¹².

S1.1 Quasi-static Mechanical Loading Process

To simulate quasi-static mechanical loading processes, we combined ADAIS¹³ and VASP to calculate the stress-strain relationships of Cs₂AgBiBr₆ using a 2×2×2 supercell. We applied tensile or pure shear strains on specific systems while allowing relaxation of the other five strain components. The stress-strain relationships obtained from DFT calculations accurately describe the material's strength, toughness, structural evolution, and other properties under various loading conditions. Consequently, it directly predicts the mechanical performance of the material. Typically, the stress-strain relationships are computed by applying incremental deformations along specified modal directions. The initial atomic basis vector matrix R is transformed into the strain vector R' using a deformation matrix:

$$R' = R \cdot (I + \varepsilon) \quad (1)$$

I is the initial lattice matrix, and ε is the corresponding strain matrix.

For the tensile deformation, the strain matrix ε is expressed as:

$$\varepsilon_{tensile} = \begin{bmatrix} \varepsilon_{xx} & 0 & 0 \\ 0 & \varepsilon_{yy} & 0 \\ 0 & 0 & \varepsilon_{zz} \end{bmatrix} \quad (2)$$

For the pure shear deformation, the strain matrix ε is expressed as:

$$\varepsilon_{pure} = \begin{bmatrix} 0 & \frac{1}{2}\varepsilon_{xy} & \frac{1}{2}\varepsilon_{xz} \\ \frac{1}{2}\varepsilon_{yx} & 0 & \frac{1}{2}\varepsilon_{yz} \\ \frac{1}{2}\varepsilon_{zx} & \frac{1}{2}\varepsilon_{zy} & 0 \end{bmatrix} \quad (3)$$

In this process, the diagonal and off-diagonal elements represent tensile and shear strain components, respectively. At each incremental step, a constant strain component is applied along a predefined direction, causing both the atomic basis vectors and all atoms to simultaneously reach a relaxed state. This process continues until the remaining five components in the Hallmann-Feynman stress tensor fall below the level of 0.1 GPa. Ultimately, the remaining non-zero stress components are considered as the

obtained stress values. To ensure the continuity of deformation, the model is optimized to its initial structure for the next incremental loading after each increment. However, it is important to emphasize that our study is not aimed at simulating the strain encountered during actual material growth processes, but rather at exploring the structural evolution of materials under extreme conditions^{14,15}.

S1.2 Optical Absorption

The dielectric function is a crucial parameter describing the optical properties of the material, and its expression is given by the formula:

$$\varepsilon(\omega) = \varepsilon_1(\omega) + \varepsilon_2(\omega) \quad (4)$$

$$\varepsilon_1(\omega) = 1 + \frac{2}{\pi} \text{P} \int_0^{\infty} \frac{\varepsilon_2(\omega')\omega'}{\omega'^2 - \omega^2 + i\eta} d\omega' \quad (5)$$

$$\varepsilon_2(\omega) = \frac{4\pi^2 e^2}{\Omega} \lim_{q \rightarrow 0} \frac{1}{q^2} \times \sum_{c,v,\mathbf{k}} 2\omega_{\mathbf{k}} \delta(E_c - E_v - \omega) |\langle c | \mathbf{e} \cdot \mathbf{q} | v \rangle|^2 \quad (6)$$

where $\varepsilon_1(\omega)$ and $\varepsilon_2(\omega)$ can be transformed through the *Kramers-Kronig (K-K) relations*¹⁶. We particularly focus on formula $\varepsilon_2(\omega)$, where c represents the conduction band, v represents the valence band, and \mathbf{k} represents the K-point. The integration over k-points, denoted as $\omega_{\mathbf{k}}$, involves summing over specific k-points and multiplying by the corresponding weighting factors. Here, E_v and E_c represent the energy of the valence band and conduction band in \mathbf{k} -space, respectively and \mathbf{e} denotes the polarization direction of photons, \mathbf{q} is the electron momentum operator. Upon obtaining the dielectric function, we can further derive optical functions such as the absorption coefficient $\alpha(\omega)$:

$$\alpha(\omega) = \frac{\sqrt{2}\omega}{2} \left[\sqrt{\varepsilon_1^2 + \varepsilon_2^2} - \varepsilon_1 \right]^{\frac{1}{2}} \quad (7)$$

These parameters hold significant importance for understanding and applying the optical properties of the material.

S2.1 $(0\bar{1}\bar{1})[01\bar{1}]$ slip system

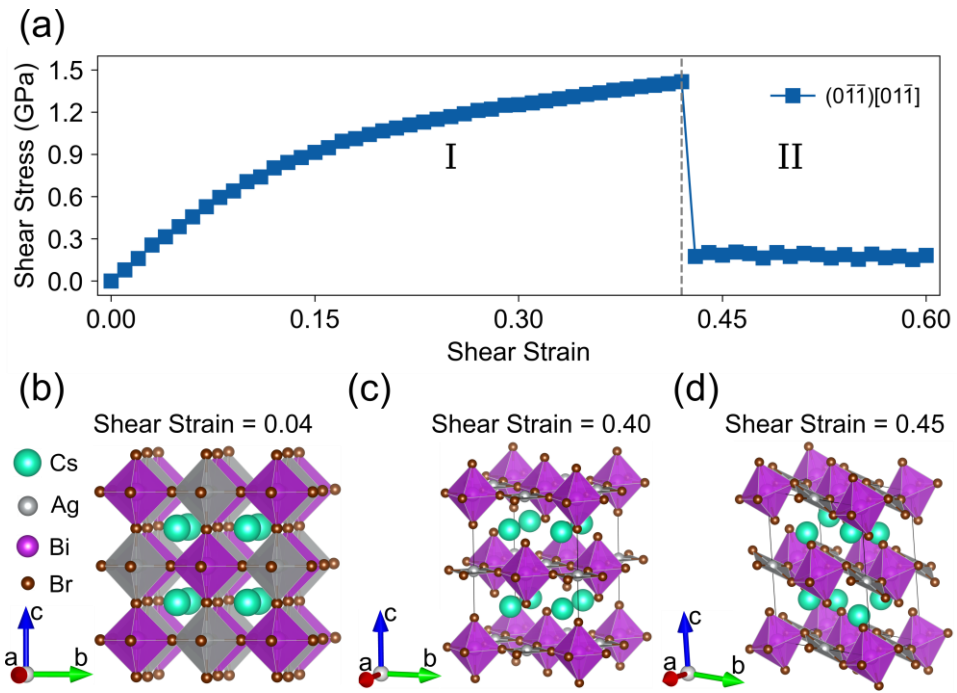


Figure S1 (a) The shear stress-strain relationship for $\text{Cs}_2\text{AgBiBr}_6$ along the $(0\bar{1}\bar{1})[01\bar{1}]$, direction. (b), (c), and (d) present the structural states of $\text{Cs}_2\text{AgBiBr}_6$ in the $(0\bar{1}\bar{1})[01\bar{1}]$ slip system at shear stresses of 0.04, 0.40, and 0.45, respectively.

S2.2 (001)[100] slip system

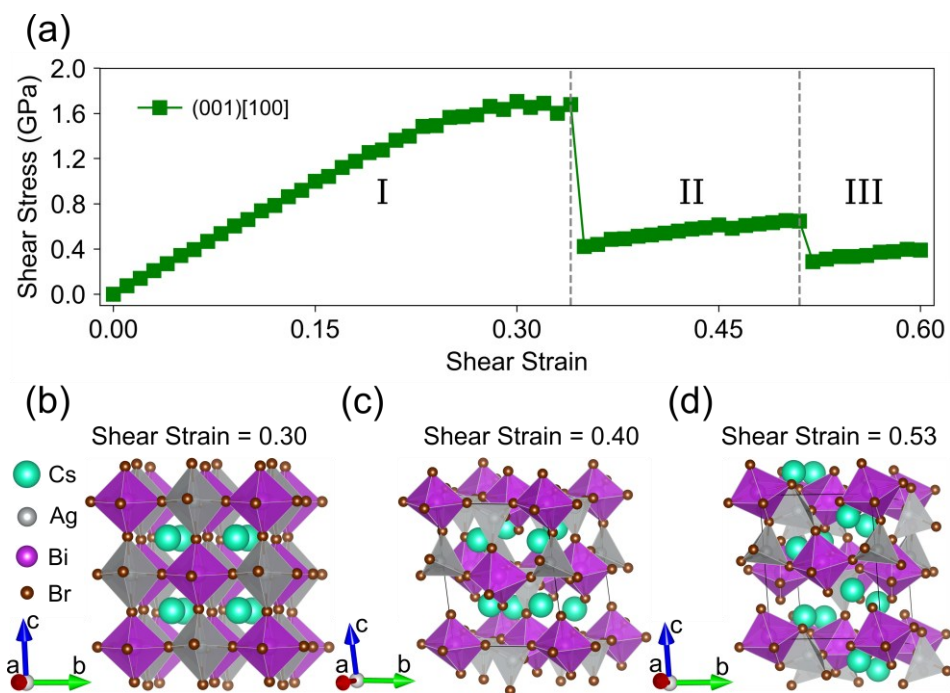


Figure S2 (a) The shear stress-strain relationship for Cs₂AgBiBr₆ along the (001)[100], direction. (b), (c), and (d) present the structural states of Cs₂AgBiBr₆ in the (001)[100] slip system at shear stresses of 0.30, 0.40, and 0.53, respectively.

S2.3 (001)[110] slip system

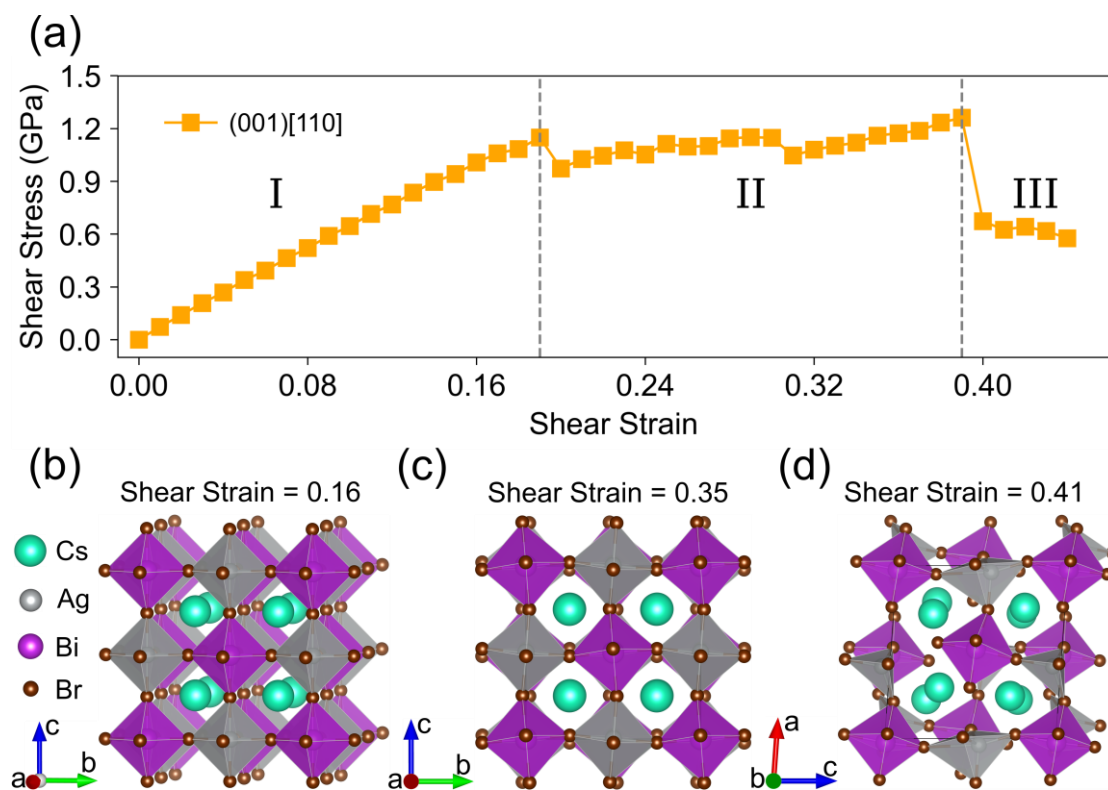


Figure S3 (a) The shear stress-shear strain relations for $\text{Cs}_2\text{AgBiBr}_6$ along the (001)[110], direction. (b), (c), and (d) present the structural states of $\text{Cs}_2\text{AgBiBr}_6$ in the (001)[110] slip system at shear stresses of 0.16, 0.35, and 0.41, respectively.

S3 Bond length analysis for Shear stress-strain process

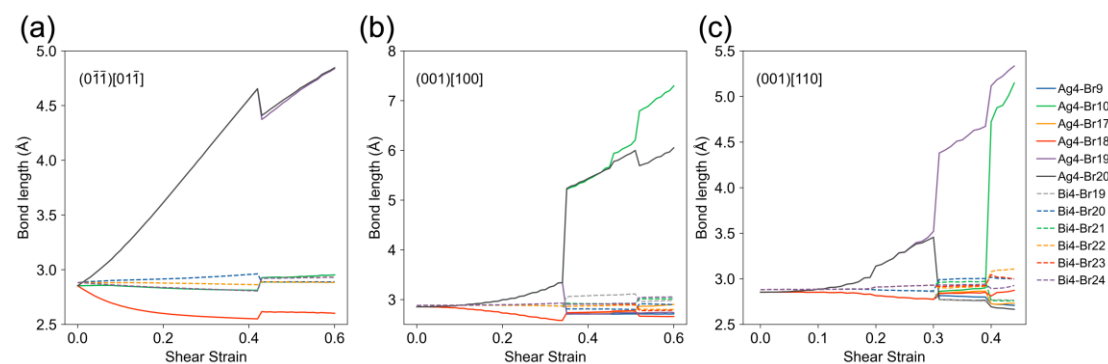


Figure S4 Variations in typical bond lengths under different shear strains. (a) $(0\bar{1}\bar{1})[01\bar{1}]$. (b) $(001)[100]$. (c) $(001)[110]$.

S4 The stability analysis of structures under large strain

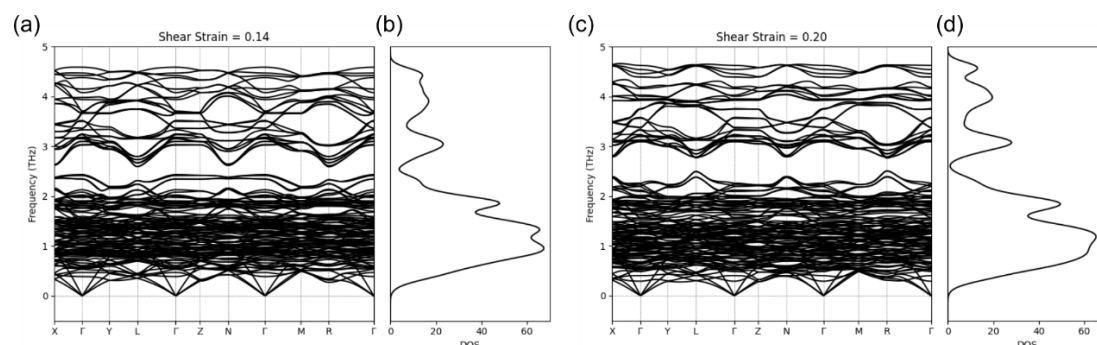


Figure S5 The phonon dispersion and total phonon density of states (DOS) at different shear strains: (a, b) 0.14, (c, d) 0.20.

S5 Ag-Br Bond Length Analysis

Here, we employed two methods to investigate the Ag-Br bond lengths. The first method involved referencing existing literature to find Ag-Br bond lengths. In this regard, we particularly focused on the Ag-Br bonds in the $(C_8H_{20}N_2)_2AgInBr_8$ structure, where the longest bond can reach 3.13 Å (the green dots in Figure S5)^{17–20}. The second method utilized structural data from existing databases. Initially, we employed spatial search algorithms (such as KD trees²¹) to find the nearest neighboring sites for each site in the Materials Project dataset²², setting distance thresholds to determine and record neighbor relationships. Subsequently, we traversed the entire structure to find the positions of Ag and Br elements and recorded their indices. Then, we systematically checked the indices of Ag (or Br) sites and matched them with the indices of neighboring Br (or Ag) sites, forming Ag-Br neighbor pairs and calculating the distances between them. Finally, we computed the average distance of all Ag-Br bonding pairs to obtain the average distance of Ag-Br bonding sites (the gray and blue dots in Figure S5). This process ensured accurate and efficient identification of all Ag-Br bonds and calculation of their average distances.

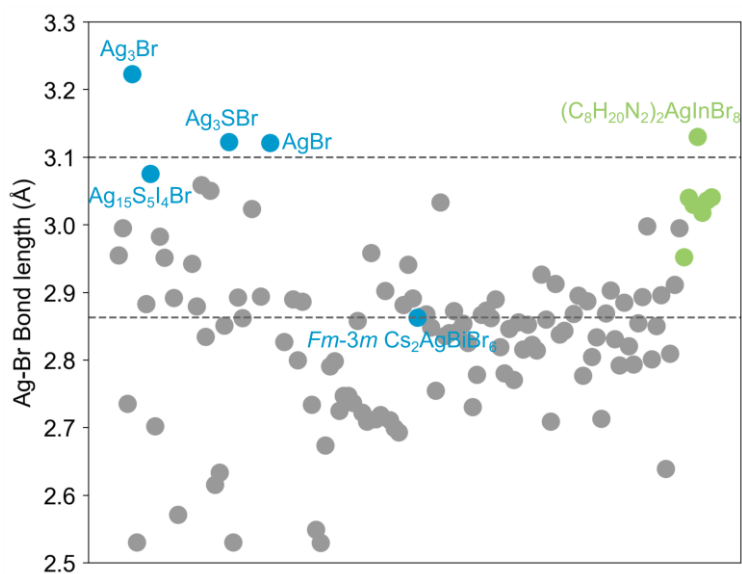


Figure S6 The bond lengths of Ag-Br bond in various compounds. The gray and blue dots data are collected from the Materials Project database, the green dots data is sourced from literature.

S6 Tensile stress–strain relations and the bond lengths Analysis

Under tension, during the initial loading stage, all tensile stresses increase linearly with the tensile strain. As the tensile stress further increases, the tensile stress in the [110] direction reaches the ideal tensile strength (1.488 GPa) first, marking the first maximum stress point. This indicates that the [110] direction is much weaker in resisting external deformation compared to the [100] and [111] directions.

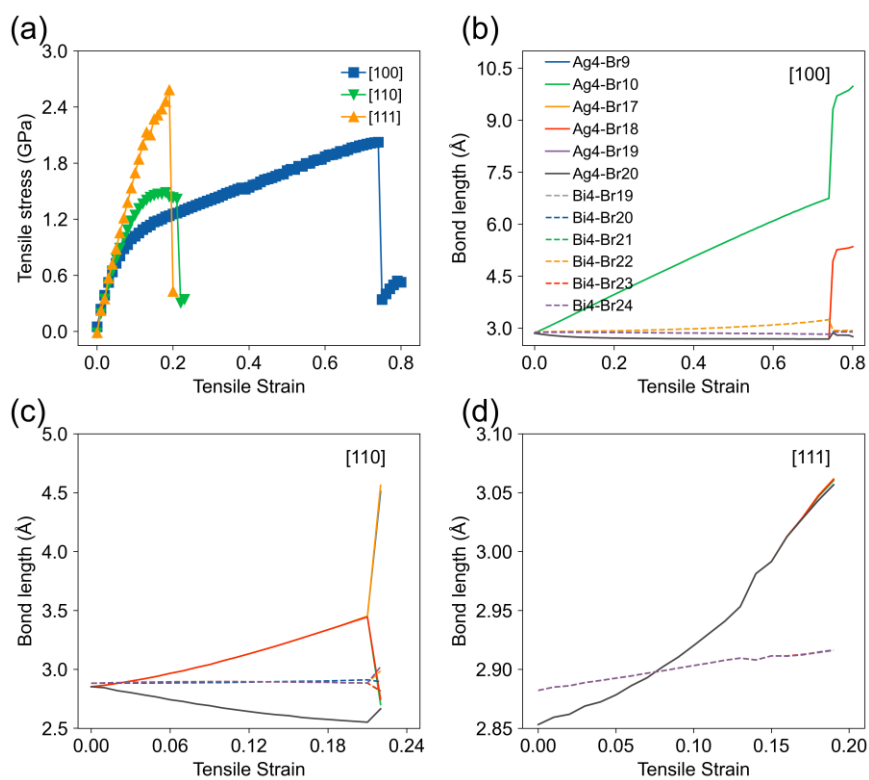


Figure S7 (a) The tensile stress-strain relationships of $\text{Cs}_2\text{AgBiBr}_6$ under biaxial tensile strain. Variations in typical bond lengths under different biaxial tensile. (a) [100]. (b) [110]. (c) [111].

S7 Vibration modes

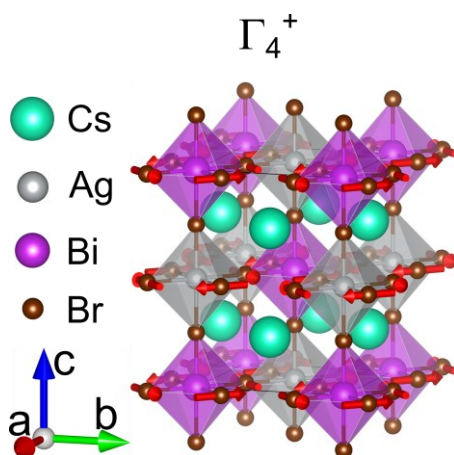


Figure S8 The Γ_4^+ vibration mode under the $Fm-3m$ to $I4/m$ phase transition

S8 The electronic structure and optical properties of $\text{Cs}_2\text{AgBiBr}_6$

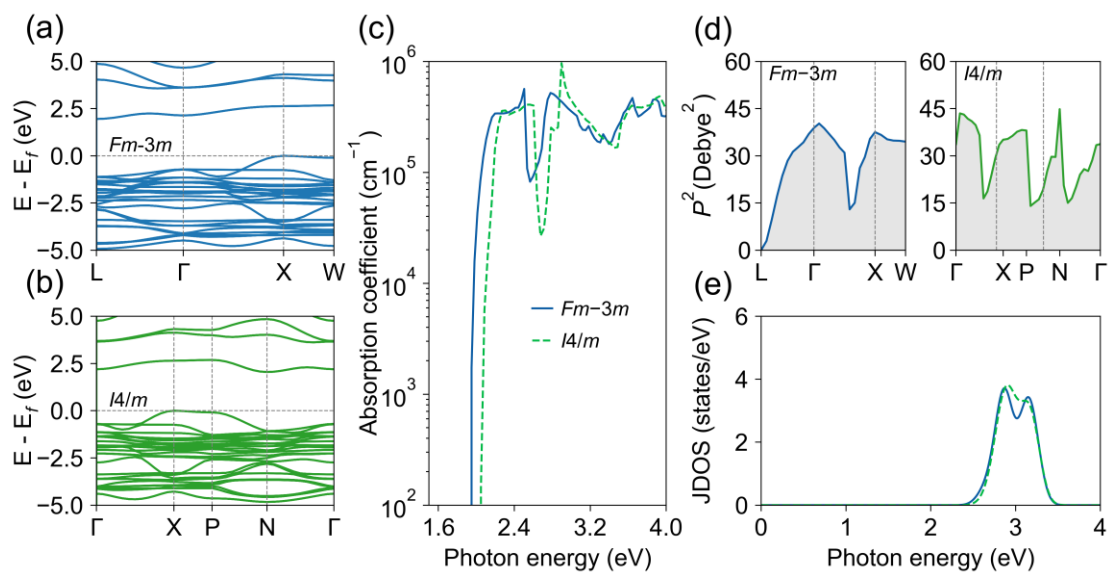


Figure S9 The band structures of $Fm-3m$ (a) and $I4/m$ (b). (c) The optical absorption spectra of $Fm-3m$ and $I4/m$. (d) Dipole transition matrix elements (P^2). (e) Joint density of states (JDOS).

References

- (1) Kresse, G.; Hafner, J. *Ab Initio* Molecular Dynamics for Open-Shell Transition Metals. *Phys. Rev. B* **1993**, *48* (17), 13115–13118. <https://doi.org/10.1103/PhysRevB.48.13115>.
- (2) Kresse, G.; Furthmüller, J. Efficiency of Ab-Initio Total Energy Calculations for Metals and Semiconductors Using a Plane-Wave Basis Set. *Comput. Mater. Sci.* **1996**, *6* (1), 15–50. [https://doi.org/10.1016/0927-0256\(96\)00008-0](https://doi.org/10.1016/0927-0256(96)00008-0).
- (3) Blöchl, P. E. Projector Augmented-Wave Method. *Phys. Rev. B* **1994**, *50* (24), 17953–17979. <https://doi.org/10.1103/PhysRevB.50.17953>.
- (4) Perdew, J. P.; Burke, K.; Ernzerhof, M. Generalized Gradient Approximation Made Simple. *Phys. Rev. Lett.* **1996**, *77* (18), 3865–3868. <https://doi.org/10.1103/PhysRevLett.77.3865>.
- (5) Heyd, J.; Scuseria, G. E.; Ernzerhof, M. Hybrid Functionals Based on a Screened Coulomb Potential. *J. Chem. Phys.* **2003**, *118* (18), 8207–8215. <https://doi.org/10.1063/1.1564060>.
- (6) Heyd, J.; Scuseria, G. E.; Ernzerhof, M. Erratum: “Hybrid Functionals Based on a Screened Coulomb Potential” [J. Chem. Phys. 118, 8207 (2003)]. *J. Chem. Phys.* **2006**, *124* (21), 219906. <https://doi.org/10.1063/1.2204597>.
- (7) Stokes, H. T.; Hatch, D. M. *FINDSYM*: Program for Identifying the Space-Group Symmetry of a Crystal. *J. Appl. Crystallogr.* **2005**, *38* (1), 237–238. <https://doi.org/10.1107/S0021889804031528>.
- (8) Baroni, S.; de Gironcoli, S.; Corso, A. D.; Giannozzi, P. Phonons and Related Properties of Extended Systems from Density-Functional Perturbation Theory. December 6, 2000. <https://doi.org/10.1103/RevModPhys.73.515>.
- (9) Ganose, A. M.; Park, J.; Faghaninia, A.; Woods-Robinson, R.; Persson, K. A.; Jain, A. Efficient Calculation of Carrier Scattering Rates from First Principles. *Nat. Commun.* **2021**, *12* (1), 2222. <https://doi.org/10.1038/s41467-021-22440-5>.
- (10) Maintz, S.; Deringer, V. L.; Tchougréeff, A. L.; Dronskowski, R. LOBSTER: A Tool to Extract Chemical Bonding from Plane-wave Based DFT. *J. Comput. Chem.*

- 2016**, 37 (11), 1030–1035. <https://doi.org/10.1002/jcc.24300>.
- (11) Deringer, V. L.; Tchougréeff, A. L.; Dronskowski, R. Crystal Orbital Hamilton Population (COHP) Analysis As Projected from Plane-Wave Basis Sets. *J. Phys. Chem. A* **2011**, 115 (21), 5461–5466. <https://doi.org/10.1021/jp202489s>.
- (12) Togo, A. First-Principles Phonon Calculations with Phonopy and Phono3py. *J. Phys. Soc. Jpn.* **2023**, 92 (1), 012001. <https://doi.org/10.7566/JPSJ.92.012001>.
- (13) Zhang, S. H.; Fu, Z. H.; Zhang, R. F. ADAIS: Automatic Derivation of Anisotropic Ideal Strength via High-Throughput First-Principles Computations. *Comput. Phys. Commun.* **2019**, 238, 244–253. <https://doi.org/10.1016/j.cpc.2018.12.012>.
- (14) Hong, S. S.; Gu, M.; Verma, M.; Harbola, V.; Wang, B. Y.; Lu, D.; Vailionis, A.; Hikita, Y.; Pentcheva, R.; Rondinelli, J. M.; Hwang, H. Y. Extreme Tensile Strain States in $\text{La}_{0.7}\text{Ca}_{0.3}\text{MnO}_3$ Membranes. *Science* **2020**, 368 (6486), 71–76. <https://doi.org/10.1126/science.aax9753>.
- (15) Du, L.; Wang, C.; Xiong, W.; Zhang, S.; Xia, C.; Wei, Z.; Li, J.; Tongay, S.; Yang, F.; Zhang, X.; Liu, X.; Liu, Q. Perseverance of Direct Bandgap in Multilayer 2D PbI_2 under an Experimental Strain up to 7.69%. *2D Mater.* **2019**, 6 (2), 025014. <https://doi.org/10.1088/2053-1583/ab01eb>.
- (16) Adachi, S. Optical Properties of $\text{In}_{1-x}\text{Ga}_x\text{As}_y\text{P}_{1-y}$ Alloys. *Phys. Rev. B* **1989**, 39 (17), 12612–12621. <https://doi.org/10.1103/PhysRevB.39.12612>.
- (17) Liu, D.; Holzapfel, N. P.; Milder, A.; Woodward, P. M. Exploring the Electronic Dimensionality of Ternary and Quaternary Rhodium Halides. *Chem. Mater.* **2024**, 36 (5), 2450–2460. <https://doi.org/10.1021/acs.chemmater.3c03208>.
- (18) Ruan, H.; Guo, Z.; Lin, J.; Liu, K.; Guo, L.; Chen, X.; Zhao, J.; Liu, Q.; Yuan, W. Structure and Optical Properties of Hybrid-Layered-Double Perovskites $(\text{C}_8\text{H}_{20}\text{N}_2)_2\text{AgMBr}_8$ (M = In, Sb, and Bi). *Inorg. Chem.* **2021**, 60 (19), 14629–14635. <https://doi.org/10.1021/acs.inorgchem.1c01669>.
- (19) Wei, F.; Deng, Z.; Sun, S.; Zhang, F.; Evans, D. M.; Kieslich, G.; Tominaka, S.; Carpenter, M. A.; Zhang, J.; Bristowe, P. D.; Cheetham, A. K. Synthesis and Properties of a Lead-Free Hybrid Double Perovskite: $(\text{CH}_3\text{NH}_3)_2\text{AgBiBr}_6$. *Chem. Mater.* **2017**, 29 (3), 1089–1094. <https://doi.org/10.1021/acs.chemmater.6b03944>.

- (20) Guo, Z.; Ruan, H.; Lin, J.; Sun, F.; Liu, K.; Chen, X.; Zhao, J.; Yuan, W. (BA)₁₀AgBi₂Br₁₉: A One-Dimensional Halide Double Perovskite with a Unique Br Trimer. *Chem. Commun.* **2022**, *58* (96), 13337–13340. <https://doi.org/10.1039/D2CC05128A>.
- (21) Beis, J. S.; Lowe, D. G. Shape Indexing Using Approximate Nearest-Neighbour Search in High-Dimensional Spaces. In *Proceedings of IEEE Computer Society Conference on Computer Vision and Pattern Recognition*; IEEE Comput. Soc: San Juan, Puerto Rico, 1997; pp 1000–1006. <https://doi.org/10.1109/CVPR.1997.609451>.
- (22) Jain, A.; Ong, S. P.; Hautier, G.; Chen, W.; Richards, W. D.; Dacek, S.; Cholia, S.; Gunter, D.; Skinner, D.; Ceder, G.; Persson, K. A. Commentary: The Materials Project: A Materials Genome Approach to Accelerating Materials Innovation. *APL Mater.* **2013**, *1* (1), 011002. <https://doi.org/10.1063/1.4812323>.